

Realistic Gottesman-Kitaev-Preskill stabilizer states enable universal quantum computation

Fariba Hosseinynejad,¹ Pavithran Iyer,² Guillaume Dauphinais,² and David L. Feder¹

¹*Institute for Quantum Science and Technology, and Department of Physics and Astronomy, University of Calgary, Calgary, Alberta, Canada T2N 1N4*

²*Xanadu Quantum Technologies Inc., Toronto, Ontario, Canada M5G 2C8*

(Dated: March 12, 2026)

Physical Gottesman-Kitaev-Preskill (GKP) states are inherently noisy as ideal ones would require infinite energy. While this is typically considered as a deficiency to be actively corrected, this work demonstrates that imperfect GKP stabilizer states can be leveraged in order to apply non-Clifford gates using only linear optical elements. In particular, Gaussian operations on normalizable GKP states, combined with homodyne measurements, permit two key primitives: clean projection onto Pauli eigenstates in the normalizable GKP codespace, thereby implementing Clifford gates with high fidelity; and probabilistic projection of unmeasured modes onto non-Pauli eigenstates. These results demonstrate that normalizable GKP stabilizer states combined with Gaussian operations provide a practical framework for computational universality within the measurement-based model of quantum computation in a realistic continuous-variable setting.

Introduction—The Gottesman-Kitaev-Preskill (GKP) codes [1] was introduced more than two decades ago, but has recently received renewed attention due to significant experimental progress in preparing, manipulating, and measuring GKP states [2–14]. The central idea is to encode a discrete-variable (DV) qubit into the continuous-variable (CV) position and momentum degrees of freedom of a harmonic oscillator, with the dual motivation of achieving intrinsic noise resilience and enabling universal quantum computation within CV architectures. Since Gaussian states combined with Gaussian operations are efficiently classically simulatable and susceptible to noise [15], GKP codes—being inherently non-Gaussian—provide a natural candidate for enabling fault-tolerant computational universality.

In the ideal square single-mode GKP encoding, logical $|0\rangle$ and $|1\rangle$ registers correspond to an infinite superposition of infinitely squeezed position eigenstates with peaks spaced by $\sqrt{\pi}$ [1], in units where $\hbar = 1$. However, these states are unphysical, as they require infinite energy. Realistic GKP states are instead constructed by introducing a Gaussian envelope over the grid peaks, effectively damping the high-photon-number components and making the states normalizable [1, 16]. We refer to these as *Fock-damped GKP states*, characterized by a single parameter controlling both the envelope and peaks width [17]. The challenge is to perform logical operations on quantum states encoded in Fock-damped GKP registers. In the ideal case, all Clifford gates correspond to Gaussian operations [1]; for example, a logical Pauli- X is simply a position quadrature displacement. However, naïve Gaussian displacements on realistic GKP states distort the envelope and reduce fidelity, requiring a more careful treatment of logical gate implementation [18]. Furthermore, to achieve universality, access to at least one non-Clifford element – either a gate or an ancillary state – is necessary.

A powerful alternative to the circuit model is *measurement-based quantum computation* (MBQC), developed in both DV [19] and CV [20] settings. MBQC replaces explicit gate sequences with adaptive local measurements on a highly entangled resource state, for example the cluster state [21–23]. Measurement-based gate teleportation is also a natural strategy for implementing both Clifford and non-Clifford operations in multimode entangled GKP states; however, previous analyses of such protocols [24] assumed ideal GKP states. In that case, only single-qubit Clifford gates can be teleported: the unmeasured modes always project onto Pauli eigenstates, rendering the circuit non-universal.

More recently, it was observed that introducing certain ancillary Gaussian states could in principle supply the missing resourcefulness [25, 26], but a complete understanding of how to practically and reliably teleport both Clifford and non-Clifford gates in a realistic setting is missing. In particular, Ref. [25] employ ideal GKP Pauli eigenstates and requires two rounds of GKP error correction on a Gaussian input, producing only one of twelve Clifford-equivalent H - or T -type magic states (rather than arbitrary states on the Bloch sphere) with less than a 10% success probability per attempt. Ref. [26] shows that circuits composed of *ideal* GKP stabilizer states, Gaussian operations, and homodyne detection are efficiently classically simulatable, and identifies the vacuum as an additional Gaussian resource that can break this simulatability. This leaves a clear knowledge gap: a resource-efficient protocol employing only realistic GKP states that enables higher-probability teleportation of genuinely non-Clifford gates, allows access to arbitrary non-Pauli states on the Bloch sphere, and avoids multiple rounds of experimentally costly GKP error correction.

A related literature has focused on identifying the resources required for universality in hybrid CV-DV settings, where the physical system is continuous-variable

but the logical layer depends on access to non-Clifford gates [15, 27]. Several works have introduced CV-to-DV mapping techniques [28, 29], combined with DV magic monotones to quantify resourcefulness [27, 30], showing that circuits of ideal GKP states, Gaussian operations, and homodyne detection are efficiently classically simulatable [25, 26, 31]. However, these analyses fundamentally rely on ideal GKP states and defer a fully realistic treatment due to the difficulty of simulating and analytically characterizing finite-squeezing effects [26, 30, 31].

In this work, we settle the open question of whether realistic, Fock-damped GKP states can enable universality by proposing a minimal, resource-efficient gate-teleportation protocol that works directly in the CV domain without invoking standard CV-to-DV mappings to quantify resourcefulness. The protocol uses a simple Gaussian circuit: two squeezed and Fock-damped GKP $|+\rangle$ states interfere on a balanced beamsplitter, followed by a phase shifter and a q -homodyne measurement. The output-state probability distribution reveals a crucial dichotomy: (1) for ideal GKP states, the protocol is limited to deterministically teleporting Clifford gates, as the unmeasured mode always projects onto a Pauli eigenstate, whereas (2) for realistic, Fock-damped GKP states, tuning the damping parameter and phase angle enables high-probability projections onto both Pauli and non-Pauli eigenstates, including magic-state-like outputs, with success probabilities ~ 0.4 for fidelities $F \gtrsim 0.96$ using experimentally relevant squeezing. We thereby establish that the finite-energy envelope of realistic GKP states, modeled here via Fock damping, becomes a resource for universal quantum computation instead of a liability.

GKP Encoding— GKP registers consist of a one-dimensional comb $|s\rangle_L = \sum_{j \in \mathbb{Z}} |(2j+s)\sqrt{\pi}\rangle_q$, $s = 0, 1$, of oscillators expressed in the position quadrature $\hat{q} = \frac{1}{2}(\hat{a} + \hat{a}^\dagger)$, where \hat{a} (\hat{a}^\dagger) are photon annihilation (creation) operators (the momentum quadrature is $\hat{p} = \frac{i}{2}(\hat{a} - \hat{a}^\dagger)$ such that the commutator is $[\hat{q}, \hat{p}] = i$). Position eigenstates are $|x\rangle_q = \sum_{n=0}^{\infty} \psi_n(x)|n\rangle$ and $\psi_n(x) = \frac{1}{\sqrt{2^n n!}} \left(\frac{1}{\pi}\right)^{1/4} e^{-x^2/2} H_n(x)$ are harmonic oscillator wave functions with $H_n(x)$ ‘physicist’ Hermite polynomials. The GKP states are non-normalizable and therefore unphysical. Realistic GKP states $|\tilde{s}\rangle_L = e^{-\beta \hat{n}} |s\rangle_L$ are finitely squeezed and Fock-damped with strength β via a Gaussian operator $\mathcal{N}_\beta = e^{-\beta \hat{n}}$, where \hat{n} is the number (Fock) operator $\hat{n} = \hat{a}^\dagger \hat{a}$; this yields logical states $|\tilde{s}\rangle_L = \sum_{j \in \mathbb{Z}} \sum_{n=0}^{\infty} \psi_n((2j+s)\sqrt{\pi}) e^{-\beta n} |n\rangle$. Throughout the remainder of this work, the logical subscript L is omitted for notational simplicity. Unless otherwise stated, all references to states such as $|0\rangle$ and $|1\rangle$ refer to their respective ideal GKP states; a tilde denotes Fock-damped normalizable physical GKP states (e.g. $|\tilde{0}\rangle$). Physically, β is set by the quality of the state-preparation process, and is not a dynamically adjustable parameter. Different values of β correspond to prepared GKP resource

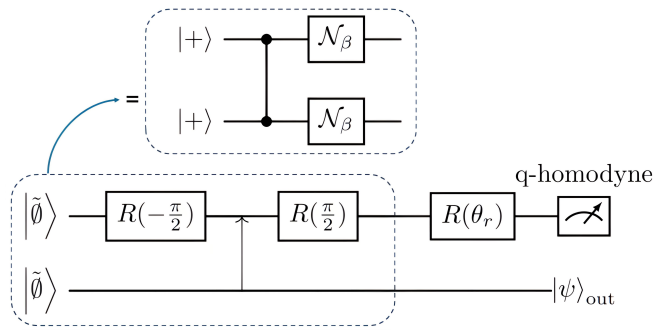


FIG. 1. Quantum circuit for gate teleportation

states with different intrinsic quality. It is important to stress that the Fock-damping operator $e^{-\beta \hat{n}}$ is used here as a convenient single-parameter model for finite-energy approximate GKP states, following Ref. [17]. Realistic preparation schemes in superconducting circuits, trapped ions, and photonics generate grid states whose Fock-space populations decay approximately as $\propto e^{-\beta n}$; the family $|\tilde{s}\rangle = e^{-\beta \hat{n}} |s\rangle$ provides an effective description of these physical states that can be approached ‘‘from below’’ by increasing the number of superposed components and the available squeezing. The Fock damping operator $e^{-\beta \hat{n}}$ is not a dynamical gate within the protocol.

Teleportation Circuit and Output State— Consider two modes $a = 1, 2$, each prepared in Fock-damped ‘sensor states’ $|\tilde{0}\rangle = \mathcal{N}_\beta |\tilde{0}\rangle$, where $|\tilde{0}\rangle = \sum_{j \in \mathbb{Z}} |j\sqrt{2\pi}\rangle_q$. These states can be subsequently entangled via a 50-50 beamsplitter BS , depicted as an arrow pointing from one mode to the other in Fig. 1, which maps $\{\hat{q}_a, \hat{p}_a\} \rightarrow \frac{1}{\sqrt{2}}\{\hat{q}_1 + (-1)^a \hat{q}_2, \hat{p}_1 + (-1)^a \hat{p}_2\}$. In practice, it is more convenient to conjugate the beamsplitter by a rotation on mode 1, so that the input state becomes [2, 24, 32, 33]

$$\begin{aligned} |\Psi\rangle_{\text{in}} &= R_{-\pi/2,1} BS_{1,2} R_{\pi/2,1} |\tilde{0}\rangle |\tilde{0}\rangle \\ &= \mathcal{N}_{\beta,1} \mathcal{N}_{\beta,2} R_{-\pi/2,1} BS_{1,2} R_{\pi/2,1} |\tilde{0}\rangle |\tilde{0}\rangle \\ &= \mathcal{N}_{\beta,1} \mathcal{N}_{\beta,2} CZ_{1,2} |+\rangle |+\rangle, \end{aligned} \quad (1)$$

where $CZ_{1,2} = e^{-i\hat{q}_1 \hat{q}_2}$ is the controlled-phase gate, the rotation operator $R_{\theta,a} = e^{i\theta \hat{n}_a}$, and $|+\rangle = \frac{1}{\sqrt{2}}(|0\rangle + |1\rangle)$. Note that the beamsplitter operator preserves the total photon number, and therefore commutes with damping operators on both modes as well as phase shifters. Thus, even though the input states are Fock-damped sensor states, the preparation circuit is mathematically equivalent to Fock-damping both modes of a cluster state of formed of entangled GKP states.

In DV case, measurement-based gate teleportation is accomplished by applying a rotation to the first qubit, followed by a computational-basis measurement; in contrast, in the CV case the rotation R_{θ_r} is applied to the first mode in quadrature (not logical) space. Applying this rotation and performing a q -homodyne measurement on the first mode with outcome q_m , as de-

picted in Fig. 1, one obtains (ignoring normalization) $|\Psi\rangle_{\text{out}} = C_+ |\bar{+}\rangle + C_- |\bar{-}\rangle$ on the second mode, where $C_+ = \cos(\theta/2)$ and $C_- = e^{i\phi} \sin(\theta/2)$ are expressed in terms of the angles defining the Bloch sphere. The coefficients C_{\pm} are derived in the Appendix:

$$C_{\pm} = \frac{e^{-i\frac{\pi}{2}k^2 \cot \zeta}}{\sqrt{1 - e^{2i\zeta}}} \sum_{j=-\infty}^{\infty} e^{-i\frac{\pi}{2}(2j+s)^2 \cot \zeta} e^{i\pi(2j+s)k \csc \zeta}, \quad (2)$$

where $s = 0, 1$ for C_+, C_- , respectively; here $\zeta \equiv \theta_r + i\beta$ and $k \equiv q_m/\sqrt{\pi}$ is a dimensionless parameter that rescales the homodyne measurement outcome q_m in natural GKP grid units. The coefficients therefore depend on the measurement outcome $q_m \rightarrow k$ as well as the adjustable parameters θ_r and β .

The coefficients can be equivalently expressed as

$$C_{\pm} = \frac{e^{i\frac{\pi}{2}k^2 \tan \zeta}}{\sqrt{2(1 + e^{2i\zeta})}} \vartheta_3 \left\{ -\frac{k\pi}{2} \sec \zeta + \frac{\pi s}{2}, e^{i\frac{\pi}{2} \tan \zeta} \right\}. \quad (3)$$

Apart from a common multiplicative factor, which is not merely a global phase since ζ is complex, the coefficients are proportional to Jacobi theta functions of the third and fourth kinds:

$$\begin{aligned} C_+ &\propto \vartheta_3 \{z, \omega\} = \vartheta_3 \{z|\tau\}; \\ C_- &\propto \vartheta_3 \left\{ z + \frac{\pi}{2}, \omega \right\} = \vartheta_4 \{z, \omega\} = \vartheta_4 \{z|\tau\}, \end{aligned} \quad (4)$$

where $z = -\frac{\pi}{2}k \sec \zeta$ and the nome which is usually represented as q is here denoted as $\omega = e^{\frac{1}{2}\pi \tan \zeta} \equiv e^{i\pi\tau}$ to prevent confusion with the position value; note that $\tau = \frac{1}{2} \tan \zeta$. The Jacobi theta functions are defined as

$$\vartheta_3 \{z, \omega\} = \sum_{\ell=-\infty}^{\infty} e^{2i\ell z} \omega^{\ell^2}; \quad \vartheta_4 \{z, \omega\} = \vartheta_3 \left\{ z + \frac{\pi}{2}, \omega \right\}. \quad (5)$$

For small but non-zero damping, $\beta \ll 1$, one may expand $\tan \zeta \approx \tan \theta_r + i\beta \sec^2 \theta_r$ to lowest order in β , such that

$$\vartheta_3 \{z, \omega\} = \sum_{\ell} e^{-\pi\beta \sec^2 \theta_r \ell^2 / 2} e^{i\pi \tan \theta_r \ell^2 / 2} e^{-2i\ell z}. \quad (6)$$

Consider the case where the applied rotation angle is obtained via the rational approximation $\tan \theta_r = u/v \in \mathbb{Q}$. In any practical setting, one can always replace $\tan \theta_r$ by a rational value consistent with its value to experimental precision, so this approximation is not overly restrictive. Then the summation above can be decomposed as $\ell = 2vm + n$, where $m, n \in \mathbb{Z}$ and $n = 0, 1, \dots, 2v - 1$. Defining the effective damping parameter $\beta' := \frac{1}{2} \left(1 + \frac{u^2}{v^2} \right) \beta$,

after some lengthy algebra one obtains

$$\begin{aligned} \vartheta_3 \{z, \omega\} &= \frac{1}{2v\sqrt{\beta'}} \sum_{n=0}^{2v-1} e^{i\pi \frac{n^2 u}{2v}} \\ &\times \sum_{\ell=-\infty}^{+\infty} e^{i\pi \ell n/v} \exp \left[-\frac{(z + \ell\pi/2v)^2}{\pi\beta'} \right], \end{aligned} \quad (7)$$

and the expression for $\theta_4(z, \omega)$ is the same other than an additional factor of $(-1)^n$ in the first sum.

Only Pauli Eigenstates Result for Zero Damping— For $\beta \rightarrow 0$ the post-measurement outcome is a Pauli eigenstate for any choice of θ_r . The results are sketched here, and additional details are provided in the Appendix. In the limit of zero damping, each Gaussian term appearing in the sum over ℓ in Eq. (7) becomes a Dirac delta function; using the identity

$$\delta(z) = \lim_{\beta \rightarrow 0} \frac{1}{\pi\sqrt{\beta}} \exp \left(-\frac{z^2}{\beta} \right), \quad (8)$$

one obtains

$$\vartheta_3 \{z, \omega\} = \frac{\pi}{2v} \sum_{n=0}^{2v-1} e^{i\pi \frac{n^2 u}{2v}} \sum_{\ell=-\infty}^{+\infty} e^{i\pi \ell n/v} \delta \left(z + \frac{\ell\pi}{2v} \right). \quad (9)$$

Therefore, the coefficients of the output state C_{\pm} are non-zero only when $z = -\frac{\ell\pi}{2v}$. In the zero-damping limit, $z \rightarrow -\pi k \sec \theta_r / 2$ and so only the values $q_m = k\sqrt{\pi}$ that will be obtained correspond to $k = \frac{\ell}{\sqrt{u^2 + v^2}} := k_m, \ell \in \mathbb{Z}$. In this limit,

$$\frac{C_-}{C_+} = \sum_{n=0}^{2v-1} e^{i\pi \frac{n^2 u}{2v}} e^{i\pi(\ell+v)n/v} \bigg/ \sum_{n=0}^{2v-1} e^{i\pi \frac{n^2 u}{2v}} e^{i\pi \ell n/v}, \quad (10)$$

i.e. the ratio of generalized quadratic Gauss sums

$$G(a, b, c) = \sum_{n=0}^{c-1} \exp \left(2\pi i \frac{an^2 + bn}{c} \right). \quad (11)$$

Using the known properties of these sums, it is straightforward to prove that the ratio C_-/C_+ is restricted to $\pm 1, \pm i$, or $\{0, \infty\}$, i.e. that the output always corresponds to Pauli eigenstates of undamped GKP basis states. In particular: if u and v are both odd, then the output is a Pauli-Y eigenstate; if u is even and v is odd then one obtains an X eigenstate; and if u is odd and v is even then the output is a Z eigenstate.

Eigenstates at Finite Damping— For small but non-zero damping, $\beta \ll 1$, one can expand z in a Taylor series to lowest order in β ; the Gaussians appearing in Eq. (7) then become

$$\exp \left[-\frac{(z + \ell\pi/2v)^2}{\pi\beta'} \right] \rightarrow e^{-(k-k_m)^2 \pi/2\beta} e^{-i\pi k(k-k_m)u/v}. \quad (12)$$

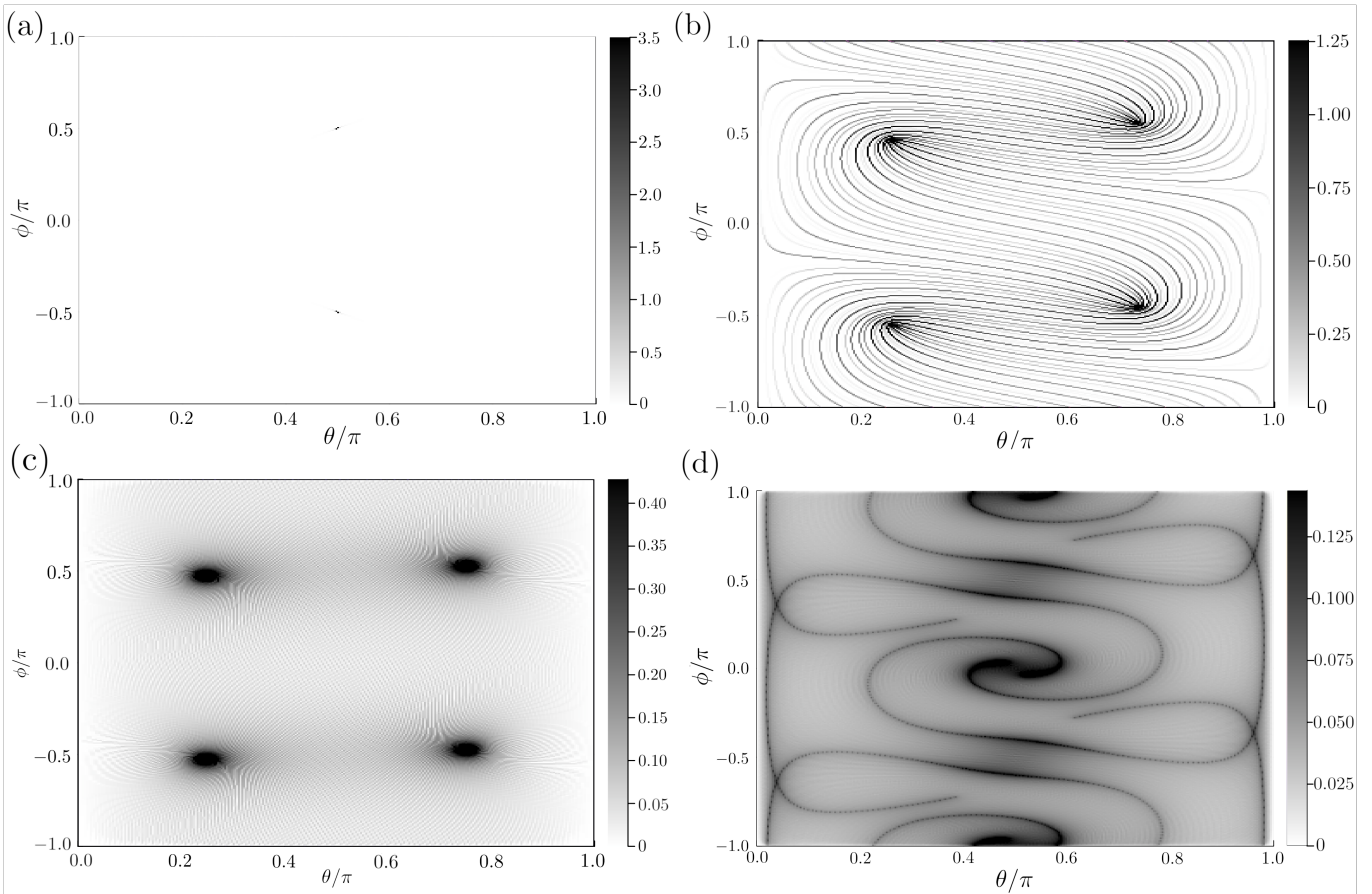


FIG. 2. Probability distribution functions for the output mode over angles θ and ϕ on the Bloch sphere. Parameters for the four panels are (a) $\beta = 0.04$ and $\theta_r = \pi/4$, and yield highly localized Pauli-Y eigenstates; (b) $\beta = 0.01$ and $\theta_r = 0.0681\pi$; (c) $\beta = 0.001$ and $\theta_r = 0.38467\pi$ yielding non-Pauli eigenstates with high probability; and (d) $\beta = 0.001$ and applied rotation angles in the range $\theta_r \in [0.38012\pi, 0.38248\pi]$ so that the four symmetry-connected points on the Bloch sphere form trajectories.

The second exponential represents a phase proportional to the distance between the measured value of rescale position quadrature k and the location k_m of the Gaussian peak; this is much smaller than the first exponential and can be ignored. For any fixed choice of either u/v or v/u , the Gaussians are highly peaked at locations $k_m = (\ell/\sqrt{(u/v)^2 + 1})/v$ or $k_m = (\ell/\sqrt{(v/u)^2 + 1})/u$. These are well-separated for sufficiently small β and value of u or v , and the output will again correspond to Pauli eigenstates. As β increases at constant v (u), or v (u) increases at constant β , the spacing between successive peaks $k_{m+1} - k_m$ decreases. The sum over ℓ in Eq. (7) will no longer be dominated by a single peak, and the output state will begin to deviate from a Pauli eigenstate. Thus, obtaining Pauli eigenstates requires a tradeoff between the peak width (governed by β) and peak separation (governed by the magnitude of u or v): a coarse rational representation of the applied phase θ_r , with $u, v \sim 1$, will almost certainly yield Pauli eigenstates for some small value of β and vice versa; whereas Pauli-state outcomes are likely to result for a finer representation of θ_r , with

$u, v \gg 1$, only for much smaller values for β .

Given the complexity introduced by the Jacobi theta functions and the non-invertible nature of the Bloch parameters $\theta(q_m)$ and $\phi(q_m)$, the final probability distributions are determined numerically without approximation (refer to the Appendix for additional details). For a fixed rotation angle θ_r , the two-mode state after Fock damping and the rotation on mode 1, and before measurement, is denoted $|\Psi_2\rangle$. A q -homodyne measurement on mode 1 with outcome q_m then occurs with probability density

$$P(q_m) = \frac{\|(\langle q_m | \otimes \mathbb{1}) |\Psi_2\rangle\|^2}{\langle \Psi_2 | \Psi_2 \rangle}. \quad (13)$$

The induced distributions on the Bloch sphere are obtained by grid-based numerical pushforward method [34]. For each value of β the symmetric homodyne window $[q_{\min}, q_{\max}]$ is adapted so that the cumulative probability inside the window satisfies $\int_{|q_m| < q_{\max}} P(q_m) dq_m \gtrsim 1 - 10^{-7}$; this guarantees that the tail probability outside the window is $P_{\text{tail}} \lesssim 10^{-7}$. The interval $[q_{\min}, q_{\max}]$ is then discretized on a dense uniform grid with spacing

$\Delta q = (\sqrt{\pi})/q_{\text{dens}}$, with typically $q_{\text{dens}} = 10^5$ points per unit $\sqrt{\pi}$. At each grid point the corresponding Bloch parameters are obtained numerically via

$$\begin{aligned}\phi &= \tan^{-1}\left(\frac{\text{Im } C_-}{\text{Re } C_-}\right) - \tan^{-1}\left(\frac{\text{Im } C_+}{\text{Re } C_+}\right), \\ \theta &= 2 \tan^{-1}\left(\frac{|C_-|}{|C_+|}\right),\end{aligned}\quad (14)$$

and a probability weight $P(q_{m,j}) \Delta q$ is assigned to that (θ, ϕ) value. Aggregating these weights over the grid yields the marginal probability density functions $g(\theta)$ and $g(\phi)$, and the two-dimensional Bloch-sphere PDFs are plotted in Fig. 2. Details of the adaptive-window criterion and grid-resolution convergence are given in the Appendix.

The theory presented above indicates that Pauli eigenstates will be overwhelmingly likely for some small but finite β and the smallest possible choices for the elements comprising the rational fraction, $u, v \in \{0, 1\}$. These correspond to rotation angles $\theta_r = n\pi/4$, $n = 0, \dots, 4$. Indeed, the PDF for $\theta_r = \pi/4$ and $\beta = 0.04$ shown in Fig. 2(a) consists of two sharp peaks on the Bloch sphere at $\theta = \pi/2$ and $\phi = \pm\pi/2$, which match to the two orthogonal Pauli-Y eigenstates, consistent with the predictions based on the Jacobi theta function analysis ($u = v = 1$, both odd). These peaks further sharpen for smaller β , and quickly become indistinguishable from a single point; even though measurement outcomes obtained away from the Gaussian maxima are not insignificant, they yield the same output states. For larger values of β , the PDF peaks become more smeared out, primarily in the θ direction. Similar results are obtained for other Pauli eigenstate outputs. Notably, this protocol permits the teleportation of all Clifford gates on Fock-damped sensor states with near unit probability for any value of $\beta \lesssim 0.04$, with no additional loss in the qubit quality.

To compare with experimental squeezing levels we convert β to an *effective per-peak squeezing in dB*. As discussed in Refs. [35, 36], the non-unitary map $\rho \mapsto e^{-\beta\hat{n}} \rho e^{-\beta\hat{n}}$ corresponds, in the Wigner representation, to convolving the state with an isotropic Gaussian kernel, which replaces each Dirac peak of the ideal GKP comb by a Gaussian peak with quadrature variance

$$\sigma^2(\beta) = \frac{1}{2} \tanh \beta. \quad (15)$$

Following the usual convention, we quote the associated per-peak squeezing relative to the vacuum variance $\sigma_{\text{vac}}^2 = \frac{1}{2}$ as

$$\Delta_{\text{dB}} = -10 \log_{10}(2\sigma^2(\beta)) = -10 \log_{10}(\tanh \beta), \quad (16)$$

so that $\Delta_{\text{dB}} > 0$ corresponds to peaks that are narrower (more squeezed) than vacuum. Thus, $\beta \approx 0.04$ corresponds to approximately 14 dB of per-peak squeezing.

Of particular interest is the possibility of obtaining non-Pauli eigenstates of damped GKP states following

this protocol. Consider the PDF shown in Fig. 2(b), with parameters $\beta = 0.01$ (20 dB of per-peak squeezing) and $\theta_r = 0.0681\pi$. The results clearly demonstrate that possible output states can be found throughout the Bloch sphere, manifested by long ‘strings’ of probability, a behavior that is found for all choices of θ_r derived from values of $u, v \gg 1$ for this value of β . For these specific parameters, significant concentration on the Bloch sphere is centered at $(\theta, \phi) \approx (\pi/4, \phi)$, close to standard magic states defined by $\theta = \pi/4, 3\pi/4$ and $\phi = \pm\pi/2$. The patterns on the Bloch sphere are located symmetrically under the following transformations (more details are provided in the Appendix): $(\theta, \phi) \rightarrow (\theta, \phi - \pi)$, $(\pi - \theta, -\phi)$, and $(\pi - \theta, \pi - \phi)$, which correspond to logical Z , X , and Y , respectively; given that the output location on the Bloch sphere is heralded from the measurement outcome through Eqs. (2) and (54), these correspond to the CV analogs of Pauli byproduct operators in MBQC. The numerical results therefore vindicate the prediction from the analytics that non-Pauli eigenstates generically result from this protocol at finite Fock damping, when $u, v \gg 1$.

Although the process is inherently probabilistic, the results remain remarkably favorable even when the Fock damping is comparatively larger ($\beta = 0.01$). As shown in Fig. 2(b), for these parameters, measurement of the first mode yields an output state with fidelity $F \gtrsim 0.94$ to one of the four Pauli-related magic states in nearly 50% of the cases. If we instead require a more stringent fidelity threshold of $F \gtrsim 0.999$, the success probability decreases to about 2%. Reducing the damping enhances this performance: for smaller β , the probability of obtaining a high-fidelity magic state ($F \gtrsim 0.999$) increases to approximately 6%, and the output distribution becomes more tightly localized around the target, as seen in Fig. 2(c) for $\beta = 0.001$ (corresponding to 30 dB of per-peak squeezing) and $\theta_r = 0.38467\pi$. These results highlight that, while the generation is not fully deterministic, tuning θ_r and the rational approximation u/v enables targeted non-Pauli outputs with high probability. Though 30 dB of squeezing exceeds current experimental capabilities, the trend clearly illustrates the strong benefits of advancing toward this regime. To highlight the practicality of this approach, even within currently feasible experimental conditions — corresponding to achievable squeezing levels of about 14 dB ($\beta = 0.04$) — approximately 40% of q -homodyne measurement outcomes yield output states with fidelity $F \gtrsim 0.96$ to one of the four Pauli-related magic states. This fidelity is well above the thresholds required for magic-state distillation protocols [37–39], indicating that the generated states are directly useful as raw resources for fault-tolerant non-Clifford gate implementation.

With sufficiently small β , almost any non-Pauli output state can be targeted with high probability by a suitable choice of θ_r . Consider, for example, $\beta = 0.001$ and $\theta_r \in [0.38012\pi, 0.38248\pi]$, an interval that includes no

Pauli output states. As the value of θ_r is varied, the localized peaks in the PDF change their positions continuously on the Bloch sphere, leaving a trajectory that is depicted in Fig. 2(d). Completely different trajectories are found by choosing different intervals. In the absence of a closed-form expression, a numerical search is required in practice to obtain the best θ_r value for a given β that yields the desired output parameters (θ, ϕ) . Although an analytic prediction of the final Bloch-sphere location remains elusive, numerical evaluation of the governing expressions identifies the attainable points for specific parameter sets, each connected to its symmetry-related counterparts through Pauli operations.

Discussion and Outlook—The analysis shows that the finite-energy envelope of realistic GKP states, modeled here via Fock damping with parameter $\beta > 0$, does not merely approximate the ideal code, or constitute a source

of noise. Rather, it supplies a key ingredient for computational universality within the framework of Gaussian operations and homodyne measurements: small but finite damping permits the teleportation of both Clifford and non-Pauli gates with high probability. These results provide a springboard to a range of promising research directions. These include: how to optimize the parameters to yield non-Pauli gates with higher fidelity; how to prepare specific non-Pauli states with high probability and fidelity at experimentally accessible squeezing levels (i.e., higher values of β); and how to extend the circuit to multiple modes in order to perform more complex gates or to optimize the parameters. These and related questions will be pursued in future work.

Acknowledgments—The authors acknowledge Mear M. R. Koochakie for his helpful discussions and numerical assistance.

Appendix

Derivation of the Output State

The initial state is taken to be

$$|\Psi_1\rangle = CZ|+\rangle|+\rangle = \frac{1}{\sqrt{2}}(|0\rangle|+\rangle + |1\rangle|-\rangle), \quad (17)$$

where $|\pm\rangle$ are ideal (undamped) sensor states (squeezed $|+\rangle$ GKP states). This can be re-expressed as

$$\begin{aligned} |\Psi_1\rangle &= \frac{1}{\sqrt{2}} \left(\sum_{j=-\infty}^{\infty} |2j\sqrt{\pi}\rangle_q|+\rangle + \sum_{j=-\infty}^{\infty} |(2j+1)\sqrt{\pi}\rangle_q|-\rangle \right) \\ &= \frac{1}{\sqrt{2}} \left(\sum_{j=-\infty}^{\infty} \sum_{n=0}^{\infty} \psi_n(2j\sqrt{\pi})|n\rangle|+\rangle + \sum_{j=-\infty}^{\infty} \sum_{n=0}^{\infty} \psi_n[(2j+1)\sqrt{\pi}]|n\rangle|-\rangle \right), \end{aligned} \quad (18)$$

where the harmonic oscillator wavefunctions are given by

$$\psi_n(x) = \frac{1}{\sqrt{2^n n!}} \pi^{-1/4} e^{-x^2/2} H_n(x) \quad (19)$$

and $H_n(x)$ are Hermite polynomials. Note that these states are not formally normalizable, but their Fock-damped counterparts below are.

Applying the rotation to the first mode via

$$e^{i\theta_r \hat{n}}|q\rangle = \sum_{n=0}^{\infty} \psi_n(q) e^{i\theta_r n} |n\rangle \quad (20)$$

and Fock damping to both modes via

$$e^{-\beta \hat{n}}|q\rangle = \sum_{n=0}^{\infty} \psi_n(q) e^{-\beta n} |n\rangle, \quad (21)$$

the state becomes

$$|\Psi_2\rangle = \frac{1}{\sqrt{2}} \left(\sum_{j=-\infty}^{\infty} \sum_{n=0}^{\infty} \psi_n(2j\sqrt{\pi}) e^{i\theta_r - \beta} |n\rangle|\tilde{+}\rangle + \sum_{j=-\infty}^{\infty} \sum_{n=0}^{\infty} \psi_n[(2j+1)\sqrt{\pi}] e^{i\theta_r - \beta} |n\rangle|\tilde{-}\rangle \right), \quad (22)$$

where $|\tilde{\pm}\rangle$ represent Fock-damped sensor states. Applying a q -homodyne measurement to the first mode yields

$$\langle q|\Psi_2\rangle = \frac{1}{\sqrt{2}} \left(\sum_{j=-\infty}^{\infty} \sum_{n=0}^{\infty} \psi_n(2j\sqrt{\pi}) e^{i\theta_r - \beta} \psi_n(q) |\tilde{+}\rangle + \sum_{j=-\infty}^{\infty} \sum_{n=0}^{\infty} \psi_n[(2j+1)\sqrt{\pi}] e^{i\theta_r - \beta} \psi_n(q) |\tilde{-}\rangle \right), \quad (23)$$

which can be alternatively expressed as

$$|\psi\rangle_{\text{out}} = \frac{1}{\mathcal{N}} \left(\langle q_m|\tilde{0}\rangle_r |\tilde{+}\rangle + \langle q_m|\tilde{1}\rangle_r |\tilde{-}\rangle \right), \quad (24)$$

where the coefficients are given by

$$\begin{aligned} \langle q_m|\tilde{s}\rangle_r &= \sum_{j=-\infty}^{+\infty} \sum_{n=0}^{\infty} \psi_n((2j+s)\sqrt{\pi}) e^{(i\theta_r - \beta)n} \psi_n(q_m), \quad s \in \{0, 1\} \\ &= \frac{e^{-q_m^2/2}}{\sqrt{\pi}} \sum_{j=-\infty}^{+\infty} e^{-(2j+s)^2\pi/2} \sum_{n=0}^{\infty} \frac{e^{(i\theta_r - \beta)n}}{2^n n!} H_n((2j+s)\sqrt{\pi}) H_n(q_m). \end{aligned} \quad (25)$$

The summation over n may be evaluated using Mehler's formula:

$$\sum_{n=0}^{\infty} \frac{H_n(q)H_n(q')}{n!} \left(\frac{w}{2}\right)^n = \frac{1}{\sqrt{1-w^2}} \exp\left(\frac{2qq'w - (q^2 + q'^2)w^2}{1-w^2}\right), \quad (26)$$

which is valid for $|w| < 1$. In the present case, $w = e^{i\theta_r - \beta}$, and the convergence condition is satisfied since $|e^{i\theta_r - \beta}| < 1$ for $\beta > 0$. Note that this work is careful to always consider finite β , and then to take the limit $\beta \rightarrow 0$. One obtains

$$\langle q_m|\tilde{s}\rangle_r \propto \frac{e^{-q^2/2} e^{-q^2/(w^{-2}-1)}}{\sqrt{1-w^2}} \sum_{j=-\infty}^{+\infty} e^{-q'^2/2} \exp\left(\frac{2qq'w - q'^2w^2}{1-w^2}\right), \quad (27)$$

where $q' = 2j\sqrt{\pi}$ and $(2j+1)\sqrt{\pi}$ for $s = 0$ and 1 , respectively, and $w = e^{i\theta_r - \beta}$. After some straightforward algebraic manipulations, one obtains

$$\langle q_m|\tilde{s}\rangle_r \propto \frac{e^{i\frac{\pi}{2}k^2 \tan \zeta}}{2(1+e^{2i\zeta})} \vartheta_3 \left\{ -\frac{k\pi}{2} \sec \zeta + s\frac{\pi}{2}, e^{i\frac{\pi}{2} \tan \zeta} \right\}, \quad (28)$$

where $k = q_m/\sqrt{\pi}$, $\zeta \equiv \theta_r + i\beta$, and ϑ_3 is the Jacobi theta function of the third kind, defined by

$$\vartheta_3\{z, \omega\} = 1 + 2 \sum_{\ell=1}^{\infty} \omega^{\ell^2} \cos(2\ell z). \quad (29)$$

Note that $\vartheta_4\{z, \omega\} = \vartheta_3\{z + \frac{\pi}{2}, \omega\}$, so that the coefficients of the output state $|\Psi\rangle_{\text{out}} = C_+|\tilde{+}\rangle + C_-|\tilde{-}\rangle$ are (ignoring common factors)

$$C_+ \propto \vartheta_3 \left\{ -\frac{k\pi}{2} \sec \zeta, e^{i\frac{\pi}{2} \tan \zeta} \right\} := \vartheta_3\{z, \omega\} = \vartheta_3\{z|\tau\}; \quad C_- \propto \vartheta_4 \left\{ -\frac{k\pi}{2} \sec \zeta, e^{i\frac{\pi}{2} \tan \zeta} \right\} := \vartheta_4\{z, \omega\} = \vartheta_4\{z|\tau\}, \quad (30)$$

where

$$z = -\frac{\pi}{2}k \sec \zeta; \quad \omega = e^{\frac{i}{2}\pi \tan \zeta} \equiv e^{i\pi\tau} \quad \Rightarrow \quad \tau = \frac{1}{2} \tan \zeta. \quad (31)$$

Symmetries of the Output State

The PDF on the Bloch sphere, shown in Fig. 2 of the main text, reveals that the output state satisfies the symmetries $(\theta, \phi) \rightarrow (\theta, \phi - \pi)$, $(\pi - \theta, -\phi)$, and $(\pi - \theta, \pi - \phi)$. These are now proven using the properties of the Jacobi theta functions.

The Jacobi theta functions defined by Eq. (29) have two other convenient representations:

$$\vartheta_3\{z, \omega\} = 1 + \sum_{\ell=1}^{\infty} \omega^{\ell^2} (e^{2i\ell z} + e^{-2i\ell z}) = \sum_{\ell=-\infty}^{\infty} \omega^{\ell^2} e^{-2i\ell z} = \sum_{\ell=-\infty}^{\infty} e^{i\pi\tau\ell^2} e^{-2i\ell z}; \quad (32)$$

and

$$\vartheta_3\{z, \omega\} = \frac{1}{\sqrt{-i\tau}} \sum_{\ell} e^{-i\pi(z/\pi\pm\ell)^2/\tau} = \frac{1}{\sqrt{-i\tau}} e^{-iz^2/\pi\tau} \sum_{\ell} e^{-i\pi\ell^2/\tau \mp 2i\ell z/\tau}. \quad (33)$$

To prove Eq. (33), rewrite Eq. (32) as follows:

$$\begin{aligned} \vartheta_3\{z, \omega\} &= \sum_{\ell} \int_{-\infty}^{\infty} e^{i\pi\tau x^2} e^{-2izx} \delta(x - \ell) dx = \int_{-\infty}^{\infty} e^{i\pi\tau x^2} e^{-2izx} \sum_{\ell} \delta(x - \ell) dx \\ &= \int_{-\infty}^{\infty} e^{i\pi\tau x^2} e^{-2izx} \sum_r e^{\pm 2i\pi r x} dx = \sum_{\ell} \int_{-\infty}^{\infty} e^{i\pi\tau x^2} e^{-2izx} e^{\pm 2i\pi\ell x} dx \\ &= \sum_{\ell} \int_{-\infty}^{\infty} e^{i\pi\tau [x^2 - 2x(z/\pi\pm\ell)/\tau]} dx. \end{aligned} \quad (34)$$

Complete the square, and perform the Gaussian integral:

$$\begin{aligned} \vartheta_3\{z, \omega\} &= \sum_{\ell} e^{-i\pi\tau(z/\pi\pm\ell)^2/\tau^2} \int_{-\infty}^{\infty} e^{i\pi\tau [x - (z/\pi\pm\ell)/\tau]^2} dx = \sum_{\ell} e^{-i\pi\tau(z/\pi\pm\ell)^2/\tau^2} \frac{1}{\sqrt{-i\tau}} \\ &= \frac{1}{\sqrt{-i\tau}} e^{-iz^2/(\pi\tau)} \sum_{\ell} e^{-i\pi\tau(\pm 2\ell z/\pi + \ell)^2/\tau^2} = \frac{1}{\sqrt{-i\tau}} e^{-iz^2/\pi\tau} \sum_{\ell} e^{-i\pi\ell^2/\tau \mp 2i\ell z/\tau}. \end{aligned}$$

which is valid as long as $\text{Im}(\tau) > 0$. In our case for $\beta \ll 1$

$$\tau = \frac{1}{2} \tan \zeta \approx \frac{1}{2} [\tan \theta_r + i\beta (1 + \tan^2 \theta_r)],$$

and so the condition is satisfied because $\beta > 0$. Finally, the Jacobi theta function is invariant on $z \rightarrow -z$. This completes the proof.

The Jacobi elliptic functions have three convenient symmetries. These are

$$\vartheta_3\{z + (m + n\tau)\pi, \omega\} = q^{-n^2} e^{-2inz} \vartheta_3\{z, \omega\}, \quad m, n \in \mathbb{Z}; \quad (35)$$

$$\vartheta_3\left\{z \pm \frac{\pi}{2} \middle| \tau\right\} = \vartheta_3\{z|\tau \pm 1\} \Leftrightarrow \vartheta_3\left\{z \pm \frac{\pi}{2} \middle| \tau \pm 1\right\} = \vartheta_3\{z|\tau\}; \quad (36)$$

$$\vartheta_3\left\{\frac{z}{\tau} \middle| -\frac{1}{\tau}\right\} = e^{iz^2/(\pi\tau)} \sqrt{-i\tau} \vartheta_3\{z|\tau\}. \quad (37)$$

Consider first symmetry (35). The case with $m \neq 0$ and $n = 0$ follows directly from Eq. (29):

$$\vartheta_3\{z + m\pi, \omega\} = 1 + 2 \sum_{\ell=1}^{\infty} \omega^{\ell^2} \cos(2\ell z + 2\ell m\pi) = \vartheta_3\{z, \omega\}.$$

The case with $m = 0$ and $n \neq 0$ is not as obvious. Using Eq. (33), the transformation $z \rightarrow z + n\pi\tau$ yields

$$\begin{aligned} \vartheta_3\{z + n\pi\tau|\tau\} &= \sqrt{\frac{\tau}{i}} e^{-i(z+n\pi\tau)^2/\pi\tau} \sum_{j=-\infty}^{\infty} e^{-i\pi j^2/\tau} e^{-2ij(z+n\pi\tau)/\tau} \\ &= \sqrt{\frac{\tau}{i}} e^{-iz^2/\pi\tau} e^{-in^2\pi\tau} e^{-2inz} \sum_{j=-\infty}^{\infty} e^{-i\pi j^2/\tau} e^{-2ijz/\tau} = \omega^{-n^2} e^{-2inz} \vartheta_3\{z|\tau\}, \end{aligned} \quad (38)$$

as needed.

Symmetry (36) again follows directly from the definition of the theta functions, Eq. (29):

$$\begin{aligned} \vartheta_3 \left\{ z \pm \frac{\pi}{2} \middle| \tau \right\} &= 1 + 2 \sum_{\ell=1}^{\infty} \omega^{\ell^2} \cos(2\ell z + \ell\pi) = 1 + 2 \sum_{\ell=1}^{\infty} (-1)^\ell \omega^{\ell^2} \cos(2\ell z) = 1 + 2 \sum_{\ell=1}^{\infty} (-\omega)^{\ell^2} \cos(2\ell z) \\ &= 1 + 2 \sum_{\ell=1}^{\infty} \left(e^{i\pi(\tau \pm 1)} \right)^{\ell^2} \cos(2\ell z) = \vartheta_3 \{ z | \tau \pm 1 \}. \end{aligned} \quad (39)$$

Note that this also implies that $\vartheta_3 \{ z \pm \frac{\pi}{2}, \omega \} = \vartheta_3 \{ z, -\omega \}$. Combining this with symmetry (35) gives

$$\vartheta_3 \left\{ z + \frac{\pi}{2} + \frac{\pi}{2} \middle| \tau \right\} = \vartheta_3 \{ z | \tau \} = \vartheta_3 \left\{ z + \frac{\pi}{2} \middle| \tau \pm 1 \right\} = \vartheta_3 \{ z | \tau \pm 2 \},$$

which implies that $\vartheta_3 \{ z | \tau \}$ is periodic on $\tau \rightarrow \tau \pm 2$. The same conclusion could also have been reached directly from the fact that $\omega = e^{i\pi\tau}$ so that $\tau \rightarrow \tau \pm 2$ maps $\omega \rightarrow \omega$.

Finally, consider symmetry (37). Using Eq. (32) one obtains

$$\vartheta_3 \left\{ \frac{z}{\tau} \middle| -\frac{1}{\tau} \right\} = \sum_{\ell} e^{-i\pi\ell^2/\tau} e^{-2i\ell z/\tau}.$$

Comparing the right-hand side with Eq. (33) immediately yields

$$\vartheta_3 \left\{ \frac{z}{\tau} \middle| -\frac{1}{\tau} \right\} = \sqrt{-i\tau} e^{iz^2/\pi\tau} \vartheta_3 \{ z | \tau \},$$

which completes the proof.

If $z \rightarrow z + \pi/2$, then $\vartheta_3 \{ z | \tau \} \rightarrow \vartheta_3 \{ z + \frac{\pi}{2} | \tau \}$, corresponding to $C_+ \rightarrow C_-$, and

$$\vartheta_3 \left\{ z + \frac{\pi}{2} \middle| \tau \right\} \rightarrow \vartheta_3 \{ z + \pi | \tau \} = \vartheta_3 \{ z | \tau + 2 \} = \vartheta_3 \{ z | \tau \},$$

using symmetry (36), corresponding to $C_- \rightarrow C_+$. Under this transformation, the new angles on the Bloch sphere become

$$\begin{aligned} \theta' &= 2 \tan^{-1} \left(\frac{|C_+|}{|C_-|} \right) = 2 \left[\frac{\pi}{2} - \tan^{-1} \left(\frac{|C_-|}{|C_+|} \right) \right] = \pi - \theta; \\ \phi' &= \tan^{-1} \left(\frac{\text{Im}(C_+)}{\text{Re}(C_+)} \right) - \tan^{-1} \left(\frac{\text{Im}(C_-)}{\text{Re}(C_-)} \right) = -\phi, \end{aligned}$$

which accounts for the mapping $(\theta, \phi) \rightarrow (\pi - \theta, -\phi)$. Because $\vartheta_3 \{ z \pm m\pi | \tau \} = \vartheta_3 \{ z | \tau \}$, it is also true that the map $\vartheta_3 \{ z | \tau \} \rightarrow \vartheta_3 \{ z + \frac{\pi}{2} | \tau \}$ is equivalent to $\vartheta_3 \{ z + 1 | \tau \} \rightarrow \vartheta_3 \{ z + \frac{\pi}{2} | \tau \}$, which is the same as $\vartheta_3 \{ z | \tau \} \rightarrow \vartheta_3 \{ z - \frac{\pi}{2} | \tau \}$. Therefore the map $C_+ \leftrightarrow C_-$ corresponds more generally to $z \rightarrow z \pm \frac{\pi}{2}$.

Using the definition of z , Eq. (31), the map $z \leftrightarrow z \pm \pi/2$ corresponds to

$$-\frac{\pi}{2} k \sec \zeta \rightarrow -\frac{\pi}{2} (k \sec \zeta \mp 1),$$

which is equivalent to $k \rightarrow k \pm \cos \zeta$. In other words, if an outcome k is obtained for some θ_r and β with high probability, then we would expect equally likely outcomes for $k \pm \cos \zeta$, or in original q units $q \pm \sqrt{\pi} \cos \zeta$. Perhaps even more important, the output state is guaranteed to repeat on the interval $q \rightarrow q \pm 2\sqrt{\pi} \cos \zeta \approx q \pm 2\sqrt{\pi} \cos \theta_r$ for any $\theta_r \gg \beta$. This observation is consistent with the high-symmetry point $\theta_r = 0$, where the output is $|+\rangle$, characterized by peaks in q space at intervals of $2n\sqrt{\pi}$ from the $|0\rangle$ state and $(2n+1)\sqrt{\pi}$ from the $|1\rangle$ state.

The only transformations that can change the relative phase of C_+ and C_- are the symmetry (35) for $n \neq 0$ and symmetry (37). Let's first consider symmetry (35), corresponding to the transformation

$$z \rightarrow z \pm n\pi\tau \quad \Leftrightarrow \quad -\frac{\pi}{2} k \sec \zeta \rightarrow -\frac{\pi}{2} k \sec \zeta \pm \frac{n\pi}{2} \tan \zeta \rightarrow -\frac{\pi}{2} \sec \zeta (k \pm n \sin \zeta), \quad (40)$$

or $k \rightarrow k \pm n \sin \zeta$. Then

$$\begin{aligned} C_+[k, \theta_r, \beta] &= \vartheta_3 \{ z, \omega \} \rightarrow \vartheta_3 \{ z + n\pi\tau, \omega \} = \omega^{-n^2} e^{-2inz} \vartheta_3 \{ z, \omega \} = e^{-i\frac{\pi}{2}n^2 \tan \zeta} e^{in\pi k \sec \zeta} C_+[k, \theta_r, \beta]; \\ C_-[k, \theta_r, \beta] &= \vartheta_3 \left\{ z + \frac{\pi}{2}, \omega \right\} \rightarrow \vartheta_3 \left\{ z + \frac{\pi}{2} + n\pi\tau, \omega \right\} = \omega^{-n^2} e^{-2in(z+\pi/2)} \vartheta_3 \left\{ z + \frac{\pi}{2}, \omega \right\} \\ &= (-1)^n e^{-i\frac{\pi}{2}n^2 \tan \zeta} e^{in\pi k \sec \zeta} C_-[k, \theta_r, \beta]. \end{aligned}$$

The new prefactors are the same for both C_+ and C_- , save for an additional $(-1)^n$ factor on C_- . For even n this maps $|\psi\rangle \rightarrow |\psi\rangle$, which implies that the measurement outcomes are invariant under $k \pm 2n \sin \zeta$ or $q \pm 2n\sqrt{\pi} \sin \theta_r$ for $\theta_r \gg \beta$. For small θ , this is a much shorter period in q than was obtained from symmetry (36). For odd n , the transformation changes the sign of both the real and imaginary parts of C_- , which has no effect on θ but maps $\phi \rightarrow \phi - \pi$ using the elementary properties of the tangent function. This recovers the map $(\theta, \phi) \rightarrow (\theta, \phi - \pi)$. Combining the results above with this one yields the third and final map $(\theta, \phi) \rightarrow (\pi - \theta, \pi - \phi)$.

In summary, if the output probability is high for outcome q , we generically expect high-probability outputs at points

$$\begin{aligned} k &\rightarrow k \pm (m \cos \zeta + n \sin \zeta) \approx k \pm (m \cos \theta_r + n \sin \theta_r), \quad n, m \in \mathbb{Z}; \\ q &\rightarrow q \pm \sqrt{\pi} (m \cos \zeta + n \sin \zeta) \approx q \pm \sqrt{\pi} (m \cos \theta_r + n \sin \theta_r), \quad n, m \in \mathbb{Z}, \end{aligned} \quad (41)$$

assuming that $\theta_r \gg \beta$.

Case where $\tan \theta_r$ is rational

Using Eqs. (31) and (32), one can write

$$\begin{aligned} \vartheta_3\{z, \omega\} &= \sum_{\ell} e^{i\pi\tau\ell^2} e^{-2i\ell z} = \sum_{\ell} e^{i\frac{\pi}{2}\ell^2 \tan \zeta} e^{-2i\ell z} = \sum_{\ell} e^{i\pi(\tan \theta_r + i\beta \sec^2 \theta_r)\ell^2/2} e^{-2i\ell z} \\ &= \sum_{\ell} e^{-\pi\beta \sec^2 \theta_r \ell^2/2} e^{i\pi \tan \theta_r \ell^2/2} e^{-2i\ell z} \end{aligned}$$

Approximate $\tan \theta_r = u/v\mathbb{Q}$, where u and v are coprime integers. In that case,

$$\sin \theta_r = \frac{u}{\sqrt{u^2 + v^2}}; \quad \cos \theta_r = \frac{v}{\sqrt{u^2 + v^2}}.$$

Then

$$\vartheta_3\{z, \omega\} = \sum_{\ell} e^{-\pi\beta(1+u^2/v^2)\ell^2/2} e^{i\pi\ell^2 u/2v} e^{-2i\ell z} \equiv \sum_{\ell} e^{-\pi\beta'\ell^2} e^{i\pi\ell^2 u/2v} e^{-2i\ell z},$$

where $\beta' := (1 + u^2/v^2)\beta/2$ is defined for convenience.

Let's decompose the sum over $\ell = 2vm + n$, where $m, n \in \mathbb{Z}$ and $n = 0, 1, \dots, 2v - 1$. Consider for example $u = 1$ and $v = 1$; then $\ell = \{2m, 2m + 1\}$ for $n = \{0, 1\}$, corresponding to summing over all even and odd integers. Breaking the sum up in this way is therefore equivalent to summing over ℓ modulo $2v$. Then

$$\begin{aligned} \vartheta_3\{z, q\} &= \sum_m \sum_{n=0}^{2v-1} e^{-\pi\beta'(2vm+n)^2} \exp\left[i\pi\left(\frac{(2vm+n)^2 u}{2v}\right)\right] e^{-2i(2vm+n)z} \\ &= \sum_m \sum_{n=0}^{2v-1} e^{-\pi\beta'(2vm+n)^2} \exp\left[i\pi\left(2mu(vm+n) + \frac{n^2 u}{2v}\right)\right] e^{-2i(2vm+n)z} \\ &= \sum_{n=0}^{2v-1} e^{i\pi\frac{n^2 u}{2v}} e^{-2inz} \sum_m e^{-\pi\beta'(2vm+n)^2} e^{2i\pi m^2 uv} e^{2i\pi mun} e^{-4ivmz} \\ &= \sum_{n=0}^{2v-1} e^{i\pi\frac{n^2 u}{2v}} e^{-2inz} \sum_m e^{-\pi\beta'(2vm+n)^2} e^{-4ivmz}, \end{aligned} \quad (42)$$

where the $e^{2i\pi m^2 uv}$ and $e^{2i\pi mun}$ terms can be neglected from the sum over m , because they are both unity for all values of m . The sum over m can be readily evaluated:

$$\begin{aligned} \vartheta_3\{z, q\} &= \sum_{n=0}^{2v-1} e^{i\pi\frac{n^2 u}{2v}} e^{-2inz} \frac{1}{2v\sqrt{\beta'}} e^{-z^2/\pi\beta'} e^{2inz} \vartheta_3\left\{\frac{n\pi}{2v} + \frac{iz}{2v\beta'}, e^{-\pi/4v^2\beta'}\right\} \\ &= \frac{1}{2v\sqrt{\beta'}} e^{-z^2/\pi\beta'} \sum_{n=0}^{2v-1} e^{i\pi\frac{n^2 u}{2v}} \vartheta_3\left\{\frac{n\pi}{2v} + \frac{iz}{2v\beta'}, e^{-\pi/4v^2\beta'}\right\}. \end{aligned} \quad (43)$$

Thus, a Jacobi theta function can be considered as a finite sum over other Jacobi theta functions. These have the parameters

$$\tilde{z} = \frac{iz}{2v\beta'} + \frac{n\pi}{2v}; \quad \tilde{\tau} = \frac{i}{4v^2\beta'},$$

so that

$$\frac{\tilde{z}}{\tilde{\tau}} = 2v(z - i\pi n\beta'); \quad -\frac{1}{\tilde{\tau}} = 4iv^2\beta'; \quad e^{-iz^2/\pi\tilde{\tau}} = e^{(z-i\pi n\beta')^2/\pi\beta'}.$$

Then, using symmetry (37), one obtains the equivalent expression

$$\begin{aligned} \vartheta_3\{z, \omega\} &= \frac{1}{2v\sqrt{\beta'}} e^{-z^2/\pi\beta'} \sum_{n=0}^{2v-1} e^{i\pi \frac{n^2 u}{2v}} 2v\sqrt{\beta'} e^{(z-i\pi n\beta')^2/\pi\beta'} \vartheta_3\left\{2v(z - i\pi n\beta'), e^{-4\pi v^2\beta'}\right\} \\ &= \sum_{n=0}^{2v-1} e^{i\pi \frac{n^2 u}{2v}} e^{-2inz} e^{-\pi n^2\beta'} \vartheta_3\left\{2v(z - i\pi n\beta'), e^{-4\pi v^2\beta'}\right\}. \end{aligned} \quad (44)$$

And:

$$\begin{aligned} \vartheta_4\{z, \omega\} &\equiv \vartheta_3\left\{z + \frac{\pi}{2}, \omega\right\} = \sum_{n=0}^{2v-1} e^{i\pi \frac{n^2 u}{2v}} e^{-2inz} e^{-2in\pi/2} e^{-\pi n^2\beta'} \vartheta_3\left\{2v\left(z + \frac{\pi}{2} - i\pi n\beta'\right), e^{-4\pi v^2\beta'}\right\} \\ &= \sum_{n=0}^{2v-1} (-1)^n e^{i\pi \frac{n^2 u}{2v}} e^{-2inz} e^{-\pi n^2\beta'} \vartheta_3\left\{2v(z - i\pi n\beta'), e^{-4\pi v^2\beta'}\right\} \end{aligned} \quad (45)$$

using symmetry (35), because $v \in \mathbb{Z}$.

Note that in expression (44), $\tau_{\text{eff}} = 4i\beta'v^2$ and $z_{\text{eff}} = 2vz$ for $n = 0$; using symmetry (35), one obtains

$$\vartheta_3\left\{2vz - 4i\beta'v^2, e^{-4\pi v^2\beta'}\right\} = e^{4\pi\beta'v^2} e^{4ivz} \vartheta_3\left\{2vz, e^{-4\pi v^2\beta'}\right\},$$

so that the $n = 2v$ term in Eq. (44) is

$$e^{i\pi \frac{4v^2 u}{2v}} e^{-4ivz} e^{-4\pi v^2\beta'} \vartheta_3\left\{2vz - 4i\pi v^2\beta', e^{-4\pi v^2\beta'}\right\} = e^{2i\pi v u} \vartheta_3\left\{2vz, e^{-4\pi v^2\beta'}\right\} = \vartheta_3\left\{2vz, e^{-4\pi v^2\beta'}\right\},$$

which coincides with the $n = 0$ term. The cycle therefore repeats; likewise, the periodicity applies to Eq. (45) because the period $2v$ is always even.

Using Eq. (34), the Jacobi theta function appearing on the right-hand side of Eq.(44) can be written as

$$\begin{aligned} \vartheta_3\{2v(z - i\pi n\beta'), e^{-4\pi v^2\beta'}\} &= \sum_{\ell=-\infty}^{\infty} \frac{1}{2v\sqrt{\beta'}} \exp\left[-\frac{[\ell\pi + 2v(z - i\pi n\beta')]^2}{4\pi v^2\beta'}\right] \\ &= \frac{1}{2v\sqrt{\beta'}} e^{2inz} e^{\pi n^2\beta'} \sum_{\ell=-\infty}^{\infty} e^{i\pi\ell n/v} \exp\left[-\frac{(z + \ell\pi/2v)^2}{\pi\beta'}\right], \end{aligned} \quad (46)$$

which for $\beta' \ll 1$ corresponds to strongly localized peaks centered at $z = \ell\pi/2v$. One therefore obtains the final expressions

$$\vartheta_3\{z, \omega\} = \frac{1}{2v\sqrt{\beta'}} \sum_{n=0}^{2v-1} e^{i\pi \frac{n^2 u}{2v}} \sum_{\ell=-\infty}^{\infty} e^{i\pi\ell n/v} \exp\left[-\frac{(z + \ell\pi/2v)^2}{\pi\beta'}\right], \quad (47)$$

corresponding to Eq. (7) in the main text, and

$$\vartheta_4\{z, \omega\} = \frac{1}{2v\sqrt{\beta'}} \sum_{n=0}^{2v-1} (-1)^n e^{i\pi \frac{n^2 u}{2v}} \sum_{\ell=-\infty}^{\infty} e^{i\pi\ell n/v} \exp\left[-\frac{(z + \ell\pi/2v)^2}{\pi\beta'}\right]. \quad (48)$$

Zero-damping limit

For $\beta' \rightarrow 0$, the Gaussians appearing in Eqs. (47) and (48) correspond to Dirac delta functions, given the definition

$$\delta(z) = \lim_{\beta \rightarrow 0} \frac{1}{\pi\sqrt{\beta}} e^{-z^2/\pi\beta};$$

one obtains

$$\vartheta_3\{2v(z - i\pi n\beta'), e^{-4\pi v^2\beta'}\} \approx \frac{\pi}{2v} e^{2inz} \sum_{\ell=-\infty}^{\infty} e^{i\pi\ell n/v} \delta(z + \ell\pi/2v).$$

Eqs. (44) and (45) can then be written as

$$C_+ \left[k, \tan^{-1} \left(\frac{u}{v} \right), 0 \right] \approx \sum_{n=0}^{2v-1} e^{i\pi \frac{n^2 u}{2v}} e^{-2inz} e^{-\pi n^2 \beta'} \frac{\pi}{2v} e^{2inz} e^{\pi n^2 \beta'} \sum_{\ell=-\infty}^{\infty} e^{i\pi\ell n/v} \delta(z + \ell\pi/2v) \quad (49)$$

$$\approx \frac{\pi}{2v} \sum_{n=0}^{2v-1} e^{i\pi \frac{n^2 u}{2v}} \sum_{\ell=-\infty}^{\infty} e^{i\pi\ell n/v} \delta(z + \ell\pi/2v);$$

$$C_- \left[k, \tan^{-1} \left(\frac{u}{v} \right), 0 \right] \approx \frac{\pi}{2v} \sum_{n=0}^{2v-1} (-1)^n e^{i\pi \frac{n^2 u}{2v}} \sum_{\ell=-\infty}^{\infty} e^{i\pi\ell n/v} \delta(z + \ell\pi/2v). \quad (50)$$

Eqs. (49) and (50) clearly show that C_+ and C_- will both be non-zero only for very specific values of z when $\beta \rightarrow 0$, i.e. for very specific measurement outcomes. Given that $z = -(\pi k/2) \sec \theta_r = -(\pi k/2) \sqrt{u^2 + v^2}/v$ in this limit, the output state is only non-zero when

$$-\frac{\pi k}{2v} \sqrt{u^2 + v^2} = -\frac{\ell\pi}{2v} \Rightarrow k = \frac{\ell}{\sqrt{u^2 + v^2}}, \ell \in \mathbb{Z}.$$

It is instructive to compare this result to Eq. (41), where the peaks in the coefficients were found to be located at

$$k \approx \frac{nu + mv}{\sqrt{u^2 + v^2}}.$$

It turns out that, indeed, the peaks in the probability appear for all integers ℓ .

Eqs. (49) and (50) together yield

$$\frac{C_- \left[\frac{\ell}{\sqrt{u^2 + v^2}}, \tan^{-1} \left(\frac{u}{v} \right), 0 \right]}{C_+ \left[\frac{\ell}{\sqrt{u^2 + v^2}}, \tan^{-1} \left(\frac{u}{v} \right), 0 \right]} \approx \frac{\sum_{n=0}^{2v-1} (-1)^n e^{i\pi \frac{n^2 u}{2v}} e^{i\pi\ell n/v}}{\sum_{n=0}^{2v-1} e^{i\pi \frac{n^2 u}{2v}} e^{i\pi\ell n/v}}.$$

Let's now show that only Pauli eigenstates result when $\beta \rightarrow 0$. Ignoring constant factors, one obtains

$$\begin{aligned} \left| \Psi \left[\frac{\ell}{\sqrt{u^2 + v^2}}, \tan^{-1} \left(\frac{u}{v} \right), 0 \right] \right\rangle_{\text{out}} &= \sum_{n=0}^{2v-1} e^{i\pi \frac{n^2 u}{2v}} e^{i\pi\ell n/v} |+\rangle + \sum_{n=0}^{2v-1} (-1)^n e^{i\pi \frac{n^2 u}{2v}} e^{i\pi\ell n/v} |-\rangle \\ &= 2 \sum_{n \in \text{even}}^{2v-2} e^{i\pi \frac{n^2 u}{2v}} e^{i\pi\ell n/v} |0\rangle + 2 \sum_{n \in \text{odd}}^{2v-1} e^{i\pi \frac{n^2 u}{2v}} e^{i\pi\ell n/v} |1\rangle \\ &= 2 \sum_{n=0}^{v-1} e^{i\pi \frac{2n^2 u}{v}} e^{2i\pi\ell n/v} |0\rangle + 2 \sum_{n=0}^{v-1} e^{i\pi \frac{(2n+1)^2 u}{2v}} e^{i\pi\ell(2n+1)/v} |1\rangle \\ &= 2 \sum_{n=0}^{v-1} e^{2i\pi \frac{n^2 u}{v}} e^{2i\pi\ell n/v} |0\rangle + 2e^{i\pi(2\ell+u)/2v} \sum_{n=0}^{v-1} e^{2i\pi \frac{n^2 u}{v}} e^{2i\pi n(\ell+u)/v} |1\rangle \\ &= 2e^{-i\pi\ell^2/2uv} \sum_{n=0}^{v-1} e^{2i\pi(n+\frac{\ell}{2u})^2 u/v} |0\rangle + 2e^{-i\pi\ell^2/2uv} \sum_{n=0}^{v-1} e^{2i\pi(n+\frac{\ell}{2u}+\frac{1}{2})^2 u/v} |1\rangle \\ &:= C_0|0\rangle + C_1|1\rangle. \end{aligned}$$

Both coefficients C_0 and C_1 have a close resemblance to generalized quadratic Gauss sums

$$G(u, \ell, v) = \sum_{n=0}^{v-1} e^{2i\pi(un^2 + \ell n)/v},$$

where $u, \ell, v \in \mathbb{Z}$ as has been assumed. The general solution depends crucially on the characteristics of u, ℓ , and v , i.e. if they are mutually prime, even, odd, etc.; so that general results are not generally straightforward to obtain. But certain cases are known analytically. For example, if $u = 0$ (no rotation) and choosing $v = 1$, then $C_+ = 1$ and $C_- = 0$ for ℓ even and vice versa for ℓ odd; this corresponds to outputs of $|+\rangle$ and $|-\rangle$, respectively, as expected.

If v is odd, then

$$G(u, \ell, v) = \varepsilon_c \sqrt{v} \left(\frac{u}{v}\right) e^{-2i\pi\overline{4u}\ell^2/v},$$

where

$$\left(\frac{u}{v}\right) = \begin{cases} 0 & u = 0 \pmod{v} \\ 1 & x^2 = u \pmod{v}, x \in \mathbb{Z}, \text{ has a solution} \\ -1 & x^2 = u \pmod{v}, x \in \mathbb{Z}, \text{ has no solution} \end{cases}$$

is the Jacobi symbol, $\overline{4u}$ is the modular inverse of $4u$, and

$$\varepsilon_c = \begin{cases} 1 & c = 1 \pmod{4} \\ i & c = 3 \pmod{4}. \end{cases}$$

It is straightforward to verify that under these assumptions

$$\sum_{n=0}^{v-1} e^{2i\pi(n + \frac{\ell}{2u} + \frac{1}{2})^2 u/v} = e^{i\pi uv/2} e^{i\pi\ell} \sum_{n=0}^{v-1} e^{2i\pi(n + \frac{\ell}{2u})^2 u/v}.$$

In this case,

$$\frac{C_1}{C_0} = e^{i\pi uv/2} e^{i\pi\ell}.$$

If u and v are both odd then $e^{i\pi uv/2} = \pm i$, with the measurement outcome ℓ changing the sign, in which case the output state is a Y eigenstate. If u is even and v is odd then $e^{i\pi uv/2} = \pm 1$, again with the measurement outcome changing the sign, in which case the output state is an X eigenstate.

The case where v is even is much trickier, and a general solution does not appear to exist. Instead, we turn to numerics. If ℓ is an even multiple of u , then $C_1 = 0$ for $v = 0 \pmod{4}$, and $C_0 = 0$ for $v = 2 \pmod{4}$. When ℓ takes other values (including odd ones), either C_0 or C_1 is zero, but the pattern is not clear. In all cases, however, the output corresponds to an eigenstate of Z . Therefore, for sufficiently small Fock damping any rational approximation to $\tan \theta_r$ leads to a Pauli eigenstate.

Damping parameter and per-peak squeezing

To compare with experimental squeezing levels, β is converted to an *effective per-peak squeezing in dB*. The non-unitary map $\rho \mapsto e^{-\beta\hat{n}}\rho e^{-\beta\hat{n}}$ corresponds, in the Wigner representation, to convolving the state with an isotropic Gaussian kernel, which replaces each Dirac peak of the ideal GKP comb by a Gaussian peak with quadrature variance

$$\sigma^2(\beta) = \frac{1}{2} \tanh \beta. \quad (51)$$

Following the usual convention, we quote the associated per-peak squeezing relative to the vacuum variance $\sigma_{\text{vac}}^2 = \frac{1}{2}$ as

$$\Delta_{\text{dB}} = -10 \log_{10}(2\sigma^2(\beta)) = -10 \log_{10}(\tanh \beta), \quad (52)$$

so that $\Delta_{\text{dB}} > 0$ corresponds to peaks that are narrower (more squeezed) than vacuum. Thus, for example, $\beta \approx 0.04$ corresponds to approximately 14 dB of per-peak squeezing.

Numerical methods and convergence checks

In this section the numerical procedures used to compute the probability density $P(q_m)$ for the q -homodyne outcome, to push this distribution forward to the Bloch-sphere coordinates (θ, ϕ) , and to evaluate success probabilities and fidelities are summarized. Convergence checks are presented with respect to (i) the homodyne window size (“tail probability”) and (ii) the grid resolution in q_m .

Adaptive homodyne window and tail probability

Given the complexity introduced by the Jacobi theta functions and the non-invertible nature of the Bloch parameters $\theta(q_m)$ and $\phi(q_m)$, the final probability distributions are determined numerically **without approximation**. For a fixed rotation angle θ_r , the two-mode state after Fock damping and the rotation on mode 1, and before measurement, is denoted $|\Psi_2\rangle$. A q -homodyne measurement on mode 1 with outcome q_m then occurs with probability density

$$P(q_m) = \frac{\|(\langle q_m | \otimes \mathbb{1}) |\Psi_2\rangle\|^2}{\langle \Psi_2 | \Psi_2 \rangle}. \quad (53)$$

The induced distributions on the Bloch sphere are obtained by grid-based numerical pushforward method [34]. For each value of β the symmetric homodyne window $[q_{\min}, q_{\max}]$ is adapted so that the cumulative probability inside the window satisfies $\int_{|q_m| < q_{\max}} P(q_m) dq_m \gtrsim 1 - 10^{-7}$; this guarantees that the tail probability outside the window is $P_{\text{tail}} \lesssim 10^{-7}$. The interval $[q_{\min}, q_{\max}]$ is then discretized on a dense uniform grid with spacing $\Delta q = (\sqrt{\pi})/q_{\text{dens}}$, with typically $q_{\text{dens}} = 10^5$ points per unit $\sqrt{\pi}$. At each grid point the corresponding Bloch parameters are obtained numerically via

$$\begin{aligned} \phi &= \tan^{-1}\left(\frac{\text{Im } C_-}{\text{Re } C_-}\right) - \tan^{-1}\left(\frac{\text{Im } C_+}{\text{Re } C_+}\right), \\ \theta &= 2 \tan^{-1}\left(\frac{|C_-|}{|C_+|}\right), \end{aligned} \quad (54)$$

and a probability weight $P(q_{m,j}) \Delta q$ is assigned to that (θ, ϕ) value. Aggregating these weights over the grid yields the marginal probability density functions $g(\theta)$ and $g(\phi)$, and the two-dimensional Bloch-sphere PDFs are plotted in Fig. 2.

For fixed damping parameter β and rotation angle θ_r , the homodyne outcome q_m is, in principle, supported on the entire real line. The numerical analysis is performed using a finite symmetric window $[q_{\min}, q_{\max}] = [-q_{\max}, q_{\max}]$ and a uniform grid $q_{m,j} = -q_{\max} + j \Delta q$ with step size Δq (see below). The corresponding discrete probabilities $P(q_{m,j}) \Delta q$ approximate the continuous density $P(q_m) dq_m$.

Rather than fixing q_{\max} a priori, the window is chosen adaptively for each β so that the probability mass outside the window is uniformly negligible. Specifically, for each parameter set (β, θ_r) , q_{\max} is increased until the discrete cumulative probability within the window satisfies

$$\int_{|q_m| < q_{\max}} P(q_m) dq_m \gtrsim 1 - 10^{-7} \quad (55)$$

This guarantees that the tail probability

$$P_{\text{tail}} = \int_{|q_m| > q_{\max}} P(q_m) dq_m \quad (56)$$

is bounded by $P_{\text{tail}} \lesssim 10^{-7}$ for all (β, θ_r) used in the figures.

In practice, q_{\max} depends primarily on β (through the overall width of the distribution). Once a conservative window satisfying Eq. (55) is determined for a given β , that window is fixed for all θ_r at the same β . Representative values are

$$\beta = 0.04 : \quad [q_{\min}, q_{\max}] \approx [-20\sqrt{\pi}, 20\sqrt{\pi}], \quad (57)$$

$$\beta = 0.001 : \quad [q_{\min}, q_{\max}] \approx [-120\sqrt{\pi}, 120\sqrt{\pi}], \quad (58)$$

in both cases satisfying $P_{\text{tail}} \lesssim 10^{-7}$.

Grid resolution in q_m

We parameterize the grid resolution by a density

$$q_dens := \frac{1}{\Delta q} \quad (\text{points per unit } \sqrt{\pi}),$$

so that $\Delta q = (\sqrt{\pi})/q_dens$. Unless otherwise stated, all main-text results use $q_dens = 100,000$, which corresponds to $\Delta q \approx 3.2 \times 10^{-5} \sqrt{\pi}$.

To verify that this discretization is sufficient, convergence checks are performed for representative parameter choices in both the moderately damped and strongly damped regimes. As a diagnostic, the success probability is used $P(F \geq F_0)$ of obtaining an output state with fidelity $F \geq F_0$ to one of the four Pauli-related magic states, with a threshold $F_0 = 0.96$.

Lower squeezing regime: $\beta = 0.04$

For $\beta = 0.04$ and $\theta_r = 0.062\pi$, the following values of $P(F \geq 0.96)$ as a function of q_dens are obtained:

q_dens	$P(F \geq 0.96)$
10,000	0.38936425216436615
30,000	0.38934146623980910
100,000	0.38933827051966047
300,000	0.38933396944982807
1,000,000	0.38932854022624835
3,000,000	0.38932918743041920
10,000,000	0.38932898550358597

(59)

The value used in the main simulations, $q_dens = 100,000$, differs from the finest grid, $q_dens = 10^7$, by

$$|P_{10^5} - P_{10^7}| \approx 9.3 \times 10^{-6},$$

corresponding to a relative change below 2.5×10^{-5} . Moreover, the results saturate as the grid is refined beyond $q_dens \approx 10^6$, with $|P_{3 \times 10^6} - P_{10^7}| \sim 2 \times 10^{-7}$. The reported probabilities are therefore converged to at least four significant digits in this regime.

Higher squeezing regime: $\beta = 0.001$

The most demanding case from the point of view of numerical resolution is the smallest damping considered, $\beta = 0.001$, where the homodyne window is widest and the interference fringes in $P(q_m)$ are the finest. For $\beta = 0.001$ and $\theta_r = 0.38467\pi$ we obtain:

q_dens	$P(F \geq 0.96)$
1,000	0.40477563394289745
3,000	0.40495869865312620
10,000	0.40477732206680450
30,000	0.40478719731072670
100,000	0.40480210345645460
300,000	0.40479583053813367
1,000,000	0.40479314835215340

(60)

Here the difference between $q_dens = 100,000$ and $q_dens = 1,000,000$ is

$$|P_{10^5} - P_{10^6}| \approx 9.0 \times 10^{-6},$$

again corresponding to a relative change of order 2×10^{-5} . The small non-monotonic variations at the 10^{-5} level reflect the interplay between sampling of very fine interference fringes and finite floating-point precision, and are well below the accuracy required for the plots in the main text.

Non-orthogonality of effective basis states

Let $|\Psi_2\rangle$ denote the two-mode state after the Fock damping and the rotation R_{θ_r} on mode 1, and *before* the q -homodyne measurement on that mode. Projecting onto $\langle q_m|$ on mode 1 yields

$$\langle q_m|\Psi_2\rangle = C_+(q_m)|\tilde{+}\rangle + C_-(q_m)|\tilde{-}\rangle,$$

where $|\tilde{\pm}\rangle$ are Fock-damped logical states. In all numerical calculations, the exact expression is used for the homodyne probability density,

$$P_q = \frac{||\langle q|\otimes\mathbb{1}|\Psi_2\rangle||^2}{\langle\Psi_2|\Psi_2\rangle} = 2\frac{|C_+|^2\langle\tilde{+}|\tilde{+}\rangle + |C_-|^2\langle\tilde{-}|\tilde{-}\rangle + 2\text{Re}[C_+^*C_-]\langle\tilde{+}|\tilde{-}\rangle}{(\langle\tilde{+}|\tilde{0}\rangle_r + \langle\tilde{-}|\tilde{1}\rangle_r)(\langle\tilde{+}|\tilde{0}\rangle_r + \langle\tilde{-}|\tilde{1}\rangle_r)}, \quad (61)$$

where $|\tilde{0}\rangle_r = R(\theta_r)|\tilde{0}\rangle$ and $|\tilde{1}\rangle_r = R(\theta_r)|\tilde{1}\rangle$ denote the Fock-damped logical GKP states on mode 1 after the rotation $R(\theta_r)$ (and analogously for their bras).

No assumption is made that $\langle\tilde{+}|\tilde{-}\rangle = 0$ at any stage but For completeness, the normalized overlap is also evaluated

$$\epsilon(\beta) = \frac{2\langle\tilde{+}|\tilde{-}\rangle}{\langle\tilde{+}|\tilde{+}\rangle + \langle\tilde{-}|\tilde{-}\rangle}$$

for the range of β used in the figures. This yields

β	$ \epsilon(\beta) $	(62)
0.10	7.56×10^{-4}	
0.04	5.88×10^{-9}	

For $\beta \leq 0.04$, the true overlap is below numerical double-precision accuracy and is therefore reported as zero.

In summary, the adaptive-window criterion Eq. (55), the grid-resolution tests in Tables (59)–(60), show that truncation of the homodyne window, discretization of q_m , do not affect the reported probability distributions or fidelities at the level of precision used in this work.

-
- | | |
|---|---|
| <p>[1] D. Gottesman, A. Kitaev, and J. Preskill, <i>Physical Review A</i> 64, 012310 (2001).</p> <p>[2] M. V. Larsen, J. E. Bourassa, S. Kocsis, J. F. Tasker, R. S. Chadwick, C. González-Arciniegas, J. Hastrup, C. E. Lopetegui-González, F. M. Miatto, A. Motamedi, <i>et al.</i>, <i>Nature</i> 642, 587 (2025).</p> <p>[3] H. Aghaee Rad, T. Ainsworth, R. N. Alexander, B. Altieri, M. F. Askarani, R. Baby, L. Banchi, B. Q. Baragiola, J. E. Bourassa, R. S. Chadwick, <i>et al.</i>, <i>Nature</i> 625, 500 (2025).</p> <p>[4] V. G. Matsos, C. H. Valahu, M. J. Millican, T. Navickas, X. C. Kolesnikow, M. J. Biercuk, and T. R. Tan, <i>Nat. Phys.</i> 21, 1664 (2025).</p> <p>[5] A. J. Brady, A. Eickbusch, S. Singh, J. Wu, and Q. Zhuang, <i>Progress in Quantum Electronics</i> 93, 100496 (2024).</p> <p>[6] J. E. Bourassa, R. N. Alexander, M. Vasmer, A. Patil, I. Tzitrin, T. Matsuura, D. Su, B. Q. Baragiola, S. Guha, G. Dauphinais, K. K. Sabapathy, N. C. Menicucci, and I. Dhand, <i>Quantum</i> 5, 392 (2021).</p> <p>[7] P. Campagne-Ibarcq, A. Eickbusch, S. Touzard, E. Zalys-Geller, N. E. Frattini, V. V. Sivak, P. Reinhold, S. Puri, S. Shankar, R. J. Schoelkopf, <i>et al.</i>, <i>Nature</i> 584, 368 (2020).</p> <p>[8] A. Eickbusch, V. Sivak, A. Z. Ding, S. S. Elder, S. R. Jha,</p> | <p>J. Venkatraman, B. Royer, S. M. Girvin, R. J. Schoelkopf, and M. H. Devoret, <i>Nature Physics</i> 18, 1464–1469 (2022).</p> <p>[9] V. V. Sivak, A. Eickbusch, B. Royer, S. Singh, I. Tsioutsios, S. Ganjam, A. Miano, B. L. Brock, A. Z. Ding, L. Frunzio, <i>et al.</i>, <i>Nature</i> 616, 50–55 (2023).</p> <p>[10] M. Kudra, M. Kervinen, I. Strandberg, S. Ahmed, M. Scigliuzzo, A. Osman, D. P. Lozano, M. O. Tholén, R. Borgani, D. B. Haviland, <i>et al.</i>, <i>PRX Quantum</i> 3, 10.1103/prxquantum.3.030301 (2022).</p> <p>[11] D. Lachance-Quirion, M.-A. Lemonde, J. O. Simoneau, L. St-Jean, P. Lemieux, S. Turcotte, W. Wright, A. Lacroix, J. Fréchette-Viens, R. Shillito, <i>et al.</i>, <i>Phys. Rev. Lett.</i> 132, 150607 (2024).</p> <p>[12] S. Konno, W. Asavanant, F. Hanamura, H. Nagayoshi, K. Fukui, A. Sakaguchi, R. Ide, F. China, M. Yabuno, S. Miki, <i>et al.</i>, <i>Science</i> 383, 289 (2024).</p> <p>[13] C. Flühmann, T. L. Nguyen, M. Marinelli, V. Negnevitsky, K. Mehta, and J. P. Home, <i>Nature</i> 566, 513–517 (2019).</p> <p>[14] B. de Neeve, T.-L. Nguyen, T. Behrle, and J. P. Home, <i>Nat. Phys.</i> 18, 296 (2022).</p> <p>[15] S. D. Bartlett, B. C. Sanders, S. L. Braunstein, and K. Nemoto, <i>Phys. Rev. Lett.</i> 88, 097904 (2002).</p> <p>[16] N. C. Menicucci, <i>Phys. Rev. Lett.</i> 112, 120504 (2014).</p> <p>[17] A. L. Grimsmo and S. Puri, <i>PRX Quantum</i> 2, 020101 (2021).</p> <p>[18] I. Tzitrin, J. E. Bourassa, N. C. Menicucci, and K. K. Sabapathy, <i>Phys. Rev. A</i> 101, 032315 (2020).</p> |
|---|---|

- [19] R. Raussendorf and H. J. Briegel, *Phys. Rev. Lett.* **86**, 5188 (2001).
- [20] N. C. Menicucci, P. van Loock, M. Gu, C. Weedbrook, T. C. Ralph, and M. A. Nielsen, *Phys. Rev. Lett.* **97**, 110501 (2006).
- [21] W. Asavanant, Y. Shiozawa, S. Yokoyama, B. Charoensombutamon, H. Emura, R. N. Alexander, S. Takeda, J. ichi Yoshikawa, N. C. Menicucci, H. Yonezawa, and A. Furusawa, *Science* **366**, 373 (2019).
- [22] M. V. Larsen, X. Guo, C. R. Breum, J. S. Neergaard-Nielsen, and U. L. Andersen, *Science* **366**, 369 (2019).
- [23] S. Yokoyama, R. Ukai, S. C. Armstrong, C. Sornphiphatphong, T. Kaji, S. Suzuki, J. ichi Yoshikawa, H. Yonezawa, N. C. Menicucci, and A. Furusawa, *Nature Photonics* **7**, 982 (2013).
- [24] B. W. Walshe, B. Q. Baragiola, R. N. Alexander, and N. C. Menicucci, *Phys. Rev. A* **102**, 062411 (2020).
- [25] B. Q. Baragiola, G. Pantaleoni, R. N. Alexander, A. Karanjai, and N. C. Menicucci, *Phys. Rev. Lett.* **123**, 200502 (2019).
- [26] C. Calcluth, A. Ferraro, and G. Ferrini, *Phys. Rev. A* **107**, 10.1103/PhysRevA.107.062414 (2023).
- [27] J. Davis, N. Fabre, and U. Chabaud, arXiv (2024), preprint arXiv:2407.18394, arXiv:2407.18394 [quant-ph].
- [28] M. H. Shaw, A. C. Doherty, and A. L. Grimsmo, *PRX Quantum* **5**, 010331 (2024).
- [29] G. Pantaleoni, B. Q. Baragiola, and N. C. Menicucci, *Physical Review Letters* **125**, 040501 (2020).
- [30] C. Calcluth, N. Reichel, A. Ferraro, and G. Ferrini, *PRX Quantum* **5**, 020337 (2024).
- [31] C. Calcluth, A. Ferraro, and G. Ferrini, *Quantum* **6**, 867 (2022).
- [32] I. Tzitrin, T. Matsuura, R. N. Alexander, G. Dauphinais, J. E. Bourassa, K. K. Sabapathy, N. C. Menicucci, and I. Dhand, *PRX Quantum* **2**, 040353 (2021).
- [33] K. Takase, F. Hanamura, H. Nagayoshi, J. E. Bourassa, R. N. Alexander, A. Kawasaki, W. Asavanant, M. Endo, and A. Furusawa, *Phys. Rev. A* **110**, 012436 (2024).
- [34] M. J. Evans and J. S. Rosenthal, *Probability and Statistics: The Science of Uncertainty* (W. H. Freeman and Company, New York, 2005).
- [35] K. Duivenvoorden, B. M. Terhal, and D. Weigand, *Physical Review A* **95**, 10.1103/physreva.95.012305 (2017).
- [36] J. Hastrup and U. L. Andersen, *Physical Review A* **108**, 10.1103/physreva.108.052413 (2023).
- [37] S. Bravyi and A. Kitaev, *Physical Review A* **71**, 022316 (2005).
- [38] A. M. Meier, B. Eastin, and E. Knill, *Quantum Info. Comput.* **13**, 195–209 (2013).
- [39] C. Jones, *Physical Review A* **87**, 042305 (2013).